ELSEVIER

Journal of Wind Engineering
and Industrial Aerodynamics 91 (2003) 1301–1328

JOURNAL OF
wind engineering
AND
industrial
aerodynamics

www.elsevier.com/locate/jweia

# A comparison of large Eddy simulations with a standard $k$–$\varepsilon$ Reynolds-averaged Navier–Stokes model for the prediction of a fully developed turbulent flow over a matrix of cubes

Y. Cheng[a], F.S. Lien[a], E. Yee[b,*], R. Sinclair[c]

[a] *Department of Mechanical Engineering, University of Waterloo, Waterloo, Ont., Canada*
[b] *Defence R&D Canada—Suffield, P.O. Box 4000, Medicine Hat, Alta., Canada T1A 8K6*
[c] *Rowan Williams Davies & Irwin Inc., Guelph, Ont., Canada*

Received 17 October 2002; received in revised form 6 March 2003; accepted 6 August 2003

**Abstract**

A fully developed turbulent flow over a matrix of cubes has been studied using the large Eddy simulation (LES) and Reynolds-averaged Navier–Stokes (RANS) [more specifically, the standard $k$–$\varepsilon$ model] approaches. The numerical method used in LES of an incompressible fluid flow was a second-order accurate, fully conservative discretization scheme. This scheme was used in conjunction with a dynamic semi-coarsening multigrid method applied on a staggered grid as proposed originally by Ham et al. (Proceedings of the Seventh Annual Conference of the Computational Fluid Dynamics Society of Canada, Halifax, Nova Scotia, Canada, 1999; J. Comput. Phys. 177 (2002) 117). The effects of the unresolved subgrid scales in LES are modeled using three different subgrid-scale models: namely, the standard Smagorinsky model; the dynamic model with time-averaging procedure (DMT); and, the localized dynamic model (LDM). To reduce the computational time, LES calculations were conducted on a Linux-based PC cluster using the message passing interface library. RANS calculations were performed using the STREAM code of Lien and Leschziner (Comp. Meth. Appl. Mech. Eng. 114 (1994) 123). The Reynolds number for the present flow simulations, based on the mean bulk velocity and the cube height, was 3800 which is in accordance with the experimental data of Meinders (Ph.D. Thesis, Faculty of Applied Sciences, Delft University of Technology, Delft, Netherlands, 1998). A comparison of predicted model results for mean flow and turbulence with the corresponding experimental data showed that both the LES and RANS approaches were able to predict the main characteristics of the mean flow in the array of cubes reasonably well. LES, particularly when used with LDM, was found to perform much

*Corresponding author. Tel.: 1-403-544-4605; fax: 1-403-544-3388.
*E-mail address:* eugene.yee@drdc-rddc.gc.ca (E. Yee).

0167-6105/$ - see front matter 
doi:10.1016/j.jweia.2003.08.001

better than RANS in terms of its predictions of the spanwise mean velocity and Reynolds stresses. Flow structures in the proximity of a cube, such as separation at the sharp leading top and side edges of the cube, recirculation in front of the cube, and the arch-type vortex in the wake are captured by both the LES and RANS approaches. However, LES was found to give a better overall quantitative agreement with the experimental data than RANS.


*Keywords:* LES; RANS; Inhomogeneous periodic flow

## 1. Introduction

Prediction of airflow around buildings is very important for the evaluation of building designs in architectural aerodynamics and wind engineering applications. A long-term goal of research in building aerodynamics is to provide a rigorous basis for understanding and estimating the forces and loadings on buildings and the characteristics of the flow patterns around buildings and within the streets between buildings. Further understanding of how much people will be buffeted by the wind flow around buildings or of the dispersion of contaminants released in built-up areas demands better insight and prediction of the flow around buildings and within the streets. The study of the flow over a matrix of cubes (resembling an array of buildings) using wind tunnel simulations can provide some fundamental understanding of various physical processes involved in building aerodynamics.

The flow pattern around a matrix of cubes in a boundary layer at a high-Reynolds (*Re*) number is influenced by a large number of parameters, such as the thickness of the boundary layer, layout of the cubes (aligned versus staggered arrays), characteristics of the approach flow, etc. There has been a substantial amount of experimental work in recent years to measure the flow around a single bluff body as well as the flow near, around, and above both small and large groups of obstacles. The complexity of the flow around an obstacle or group of obstacles has been recognized, and a number of characteristic patterns in this flow has been identified and investigated in detail. For example, for a sheared wind flow incident on an obstacle, the flow around the obstacle consists of a horseshoe vortex system which is responsible for creating a downwash on the front face of the obstacle and the region of reversed flow in front of the obstacle. Furthermore, there is a separation of the flow on the sharp leading top and side edges of the obstacle, and a wake recirculation zone in the lee of the obstacle [1,2]. For the case of an obstacle placed in a fully developed channel flow, the number of parameters influencing the flow are reduced, and the flow can be considered to depend primarily on the height of the channel and the Reynolds number based on the mean bulk velocity and the cube height [3]. Recently, a matrix of cubes placed in a fully developed channel flow has been investigated experimentally by Meinders et al. [4,5]. The extensive experimental data obtained in this investigation, which included mean velocity components and various

second moments of velocity, were made available as a test case—Case 6.2—for the 8th ERCOFTAC[1] workshop on turbulence modeling held at Helsinki University of Technology in 1999 [6].

With the recent rapid advances in computer technology, computational fluid dynamics (CFD) has been applied more and more to complex flows of industrial relevance. The most widely used approach in industry for the modeling of turbulent flows is Reynolds-averaged Navier–Stokes (RANS) methods. This approach assumes that non-convective transport in a turbulent flow is governed by stochastic three-dimensional turbulence possessing a broad-band spectrum with no distinct frequencies. The model must represent a very wide range of scales with the smallest scales being influenced by the fluid viscosity. This approach has obvious weaknesses and poses serious uncertainties in flows for which large-scale organized features dominate, such as flows around building-like obstacles.

Against this background, it may be argued that a sound, although computationally expensive, approach to resolving flows in which large-scale organized structures and internally or externally induced periodicity are influential is by means of large Eddy simulation (LES) of the flow. In LES, the large scales containing most of the energy are resolved explicitly, while the small scales containing a small fraction of the energy are modeled. LES can be used for two major purposes: firstly, to predict practically relevant and fundamentally interesting turbulent flows featuring organized structures, and secondly, to assess the ability of different RANS models to provide a credible representation of flow of this type. Several numerical studies, using either RANS and/or LES for prediction of a flow over or around a single obstacle in a channel or boundary layer, were reported previously [7–9]. Rodi [10] compared the performance of LES and RANS approaches for the flow past a surface-mounted cubical obstacle in a channel, and concluded that RANS models, including the standard $k$–$\varepsilon$ model applied with wall functions and the two-layer $k$–$\varepsilon$ model with the Kato–Launder turbulence production modification [11], over-predict the separation length by about 35–110%. In contrast, LES with the standard Smagorinsky subgrid model only slightly over-predicts the separation length by about 7%. The computational cost associated with LES is much greater than RANS, however—about 640 times greater than the $k$–$\varepsilon$ model applied with wall functions and 26 times greater than the two-layer $k$–$\varepsilon$ model.

In LES, the standard Smagorinsky model (SMG) remains very widely used due to its algorithmic simplicity and numerical stability. However, the major drawback associated with this model is that the optimal model parameter is flow-dependent and ad hoc modifications of this parameter are required near solid surfaces (e.g., by introducing a Van Driest-type damping function similar to that used in the mixing-length eddy-viscosity model [12]). The dynamic subgrid-scale model, originally proposed by Germano et al. [13], eliminates some of these disadvantages by determining the "Smagorinsky constant", $C_s$, as a function of time and position dynamically. Depending on the flow problem, different averaging procedures are required to ensure numerical stability. The space-averaging method [14] is commonly

[1] European Research Community on flow, turbulence and combustion.

used for flows in which homogeneity, at least in one direction, exists. This requirement precludes the possibility of computing inhomogeneous flows. For inhomogeneous flows, the model coefficient should be a function of all spatial and temporal coordinates. Akselvoll and Moin [15] proposed a simple time-averaging procedure in conjunction with space-averaging in the spanwise (homogeneous) direction to determine Smagorinsky's constant for a backward-facing-step flow. Breuer and Rodi [16] applied the same time-averaging procedure for a flow through a 180° square-sectioned duct, in which no homogeneous direction exists. Piomelli and Liu [17] proposed a new dynamic localized model, which is less rigorous but computationally more efficient than that proposed by Ghosal et al. [18], and applied it to simulate rotating channel flows.

The objective of this work is to assess the predictive performance of LES with various dynamic subgrid-scale models for a fully developed turbulent flow around a matrix of cubes. Our ultimate goal is to apply LES to a developing urban flow at a high Reynolds number. In the present study, the time-averaging procedure and localized dynamic model are adopted, since no homogeneous direction exists in the present flow. In order to compare our results with some previous investigations, simulations using the Smagorinsky subgrid-scale model with a fixed constant $C_s = 0.1$ were also performed. As a complementary effort, the same flow was computed using a RANS model (more specifically, the standard $k$–$\varepsilon$ model). The results obtained with both LES and RANS, in comparison with the experimental data of Meinders et al. [5,19], represent a comprehensive analysis of this flow and provide an opportunity to assess the relative benefits and drawbacks of the various numerical simulation technologies.

## 2. Governing equations

### 2.1. LES

When the Navier–Stokes and continuity equations for incompressible flow are filtered, one obtains

$$\frac{\partial \bar{u}_i}{\partial x_i} = 0, \tag{1}$$

$$\frac{\partial \bar{u}_i}{\partial t} + \frac{\partial \bar{u}_i \bar{u}_j}{\partial x_j} = -\frac{1}{\rho}\frac{\partial \bar{p}}{\partial x_i} - \frac{\partial}{\partial x_j}\underbrace{(\overline{u_i u_j} - \bar{u}_i \bar{u}_j)}_{\tau_{ij}}, \tag{2}$$

where $\bar{u}_i$ denotes the spatially filtered velocity components with $\bar{u}_1$ in the streamwise $x_1 \equiv x$, $\bar{u}_2$ in the wall-normal $x_2 \equiv y$, and $\bar{u}_3$ in the spanwise $x_3 \equiv z$ directions, respectively; $\bar{p}$ is the filtered pressure; and, $\rho$ is the fluid density. In the context of LES, $\tau_{ij}$ in Eq. (2) is the subgrid-scale stress tensor that is associated with the large-scale (resolved) momentum flux caused by the action of the small (unresolved) scales, and as such needs to be modeled. The most common class of subgrid models for $\tau_{ij}$ is

an eddy viscosity type with the following form:

$$\tau_{ij} - \frac{1}{3}\tau_{kk}\delta_{ij} = v_t\left(\frac{\partial \bar{u}_i}{\partial x_j} + \frac{\partial \bar{u}_j}{\partial x_i}\right) \equiv -2v_t\bar{S}_{ij}, \tag{3}$$

where $v_t$ is the eddy viscosity

$$v_t = C\bar{\Delta}^2|\bar{S}|. \tag{4}$$

Here, $\bar{\Delta}$ is the filter length scale, $|\bar{S}| \equiv (2\bar{S}_{ij}\bar{S}_{ij})^{1/2}$ and $C$ is the model parameter. A number of different methods have been used to specify $C$.

In the SMG modified to include the presence of surfaces, $C$ is determined from

$$C = C_s^2[1 - \exp(-(y^+/A^+)^3)], \tag{5}$$

where $y^+ \equiv yu_\tau/v$ is distance from the wall in viscous wall units, $u_\tau$ is the friction velocity, $v$ is the kinematic viscosity, $A^+ \approx 26$ is a dimensionless constant, and $C_s \approx 0.1$ is the Smagorinsky constant. Note that Eq. (5) incorporates an exponential van Driest damping function whose purpose is to reduce the subgrid-scale eddy viscosity near the wall. Strictly speaking, this empirical correction for $C$ is applicable to some simple flows only where the important characteristics of the near-wall turbulence are known a priori.

The model parameter $C$ should depend on the local properties of the flow and may be a function of the Reynolds number. As a consequence, dynamic procedures have been developed to diagnose a local value for $C$ (which can be a spatially and temporally varying quantity). Here, the model parameter $C$ is computed, at every spatial grid point in the flow domain and at every time step, from the results of the LES itself. We do not describe the dynamic procedure here, but simply refer the interested reader to Germano et al. [13] for the details. Although the dynamic procedure improves on the SMG, it can result in large negative values of the model parameter over extended regions of the flow domain. In turn, this gives rise to an unphysical backscatter of energy (viz., energy transfer from small scales to the large ones) that tends to destabilize the numerical simulation. A number of methods have been proposed to "cure" this problem, which usually involve an averaging of the model parameter in either space or time. However, in the current problem, no homogeneous direction exists for averaging in space so we employ an averaging in time to calculate a smoothed value for the model parameter. To this purpose, we consider two different averaging in time procedures for the regularization of the model parameter; namely, the dynamic model with time averaging (DMT) proposed by Akselvoll and Moin [15], and the localized dynamic method (LDM) proposed by Piomelli and Liu [17].

### 2.2. RANS

There are numerous RANS models, but in this paper we will consider only the standard $k$–$\varepsilon$ model (which is perhaps the most widely used RANS model). The Reynolds-averaged equations for continuity and momentum for steady,

incompressible flow are as follows:

$$\frac{\partial U_i}{\partial x_i} = 0, \tag{6}$$

and

$$\frac{\partial (U_i U_j)}{\partial x_j} = -\frac{1}{\rho}\frac{\partial P}{\partial x_i} + \frac{\partial}{\partial x_j}\left(\nu \frac{\partial U_i}{\partial x_j} - \overline{u_i' u_j'}\right). \tag{7}$$

Here, $U_i$ and $u_i'$ are the mean and fluctuating velocities in the $x_i$-direction, respectively, and $P$ is the mean pressure. The presence of the Reynolds stresses, $\overline{u_i' u_j'}$, in Eq. (7) implies that the latter are not closed. The Reynolds averaging of a quantity is denoted by drawing a bar over that quantity. Closure requires that some approximations be made in prescribing the Reynolds stresses in terms of the mean flow quantities. The most popular statistical turbulence closure model is the Boussinesq type of eddy viscosity approximation that assumes a linear relationship between the turbulent stresses and the mean velocity gradients:

$$-\overline{u_i' u_j'} = \nu_t^* \left(\frac{\partial U_i}{\partial x_j} + \frac{\partial U_j}{\partial x_i}\right) - \frac{2}{3} k \delta_{ij}, \tag{8}$$

where $\nu_t^*$ is the kinematic eddy viscosity and $k \equiv \frac{1}{2}\overline{u_i' u_i'}$ is the turbulence kinetic energy (TKE).

In the standard $k$–$\varepsilon$ model, $\nu_t^*$ is determined as

$$\nu_t^* = C_\mu \frac{k^2}{\varepsilon}, \tag{9}$$

where $\varepsilon$ is the dissipation of TKE. The standard model uses the following transport equations for $k$ and $\varepsilon$:

$$\frac{\partial (U_j k)}{\partial x_j} = \frac{\partial}{\partial x_j}\left[\left(\nu + \frac{\nu_t^*}{\sigma_k}\right)\frac{\partial k}{\partial x_j}\right] + \nu_t^* \left(\frac{\partial U_i}{\partial x_j} + \frac{\partial U_j}{\partial x_i}\right)\frac{\partial U_i}{\partial x_j} - \varepsilon, \tag{10}$$

and

$$\frac{\partial (U_j \varepsilon)}{\partial x_j} = \frac{\partial}{\partial x_j}\left[\left(\nu + \frac{\nu_t^*}{\sigma_\varepsilon}\right)\frac{\partial \varepsilon}{\partial x_j}\right] + C_{\varepsilon 1}\frac{\varepsilon}{k}\nu_t^* \left(\frac{\partial U_i}{\partial x_j} + \frac{\partial U_j}{\partial x_i}\right)\frac{\partial U_i}{\partial x_j} - C_{\varepsilon 2}\frac{\varepsilon^2}{k}. \tag{11}$$

The equations contain five closure constants: namely, $C_\mu$, $\sigma_k$, $\sigma_\varepsilon$, $C_{\varepsilon 1}$, and $C_{\varepsilon 2}$. The standard $k$–$\varepsilon$ model employs values for constants that are determined by a comprehensive data fitting over a wide range of canonical turbulent flows:

$$C_\mu = 0.09; \quad \sigma_k = 1.00; \quad \sigma_\varepsilon = 1.30; \quad C_{\varepsilon 1} = 1.44; \quad C_{\varepsilon 2} = 1.92. \tag{12}$$

The turbulent diffusion of $k$ and $\varepsilon$ in Eqs. (10) and (11), respectively, are represented using a gradient diffusion hypothesis with the Prandtl numbers $\sigma_k$ and $\sigma_\varepsilon$ used to connect the eddy diffusivities of $k$ and $\varepsilon$ to the eddy viscosity $\nu_t^*$.

## 3. Numerical method

### 3.1. LES

The discretization of the filtered Navier–Stokes and continuity equations was accomplished using a fully conservative finite-volume method on a staggered, structured and orthogonal grid. All spatial derivatives were approximated by the second-order central differencing scheme and time advancement was handled with the second-order Crank–Nicholson method. The second-order differencing and averaging operators in the $x$-direction, for example, on a structured Cartesian grid with non-uniform spacing are defined as

$$\left.\frac{\delta_1\phi}{\delta_1 x}\right|_{i,j,k,n} \equiv \frac{\phi^n_{i+1/2,j,k} - \phi^n_{i-1/2,j,k}}{x_{i+1/2} - x_{i-1/2}}, \tag{13}$$

$$\left.\bar{\phi}^{1x}\right|_{i,j,k,n} \equiv \frac{\phi^n_{i+1/2,j,k} + \phi^n_{i-1/2,j,k}}{2}, \tag{14}$$

and

$$\left.\bar{\phi}^{1\breve{x}}\right|_{i,j,k,n} \equiv \frac{(x_{i+1/2} - x_i)\phi^n_{i+1/2,j,k} + (x_i - x_{i-1/2})\phi^n_{i-1/2,j,k}}{x_{i+1/2} - x_{i-1/2}}, \tag{15}$$

where $\phi$ represents a discrete variable, and $[i, j, k, n]$ are associated with mesh indices in the $x$-, $y$-, $z$- and $t$-directions, respectively. Note that the stencil size, indicated by the "1" subscript associated with $\delta$, is always 1 in order to be consistent with the more general definitions proposed by Morinishi et al. [20].

Using the discrete operators defined above, the continuity equation is evaluated at the cell-centered location $[i, j, k, n+1]$:

$$\frac{\delta_1 u_i}{\delta_1 x_i} = 0. \tag{16}$$

The $x$, $y$ and $z$ components of the momentum equation are evaluated at the staggered locations $[i+1/2, j, k, n+1/2]$, $[i, j+1/2, k, n+1/2]$ and $[i, j, k+1/2, n+1/2]$, respectively, using the following discretization:

$$\frac{\delta_1 u_i}{\delta_1 t} + \frac{\delta_1 \overline{\overline{u_j}^{1t}}^{1\breve{x}_i} \overline{\overline{u_i}^{1t}}^{1x_j}}{\delta_1 x_j} + \frac{\delta_1 p}{\delta_1 x_i} - \frac{\delta_1 \tau_{ij}}{\delta_1 x_j} = 0, \tag{17}$$

$$\tau_{ij} = \bar{\nu}\left(\frac{\delta_1 \overline{u_i}^{1t}}{\delta_1 x_j} + \frac{\delta_1 \overline{u_j}^{1t}}{\delta_1 x_i}\right), \tag{18}$$

$$\bar{\nu} = \begin{cases} \nu & \text{for } i = j \\ \overline{\bar{\nu}^{1x_i}}^{1x_j} & \text{for } i \neq j. \end{cases} \tag{19}$$

Note that $x_i$ appearing as a superscript does not follow the summation convention. Clearly, both the mass and momentum equations are in the discrete form of Eqs. (1)

and (2). Ham et al. [21] show that the scheme discretely conserves mass, momentum, and kinetic energy (in the inviscid limit) in both space and time.

Solution of the non-linear equation sets, Eqs. (16) and (17), is based on the symmetric coupled Gauss Seidel (SCGS) method, originally proposed by Vanka [22]. SCGS cycles through all cells in the domain, correcting in each cell the six face velocities and one pressure based on a coupled solution of the six momentum equations and one continuity equation (seven equations) associated with the cell.

The efficiency of this scheme is improved by introducing the multigrid method with the dynamic semi-coarsening strategy [23]. The code is also parallelized on a Linux-based PC cluster using the message passing interface (MPI) library.

### 3.2. RANS

The RANS solutions to follow have been obtained with the flow code STREAM [24]. It employs a fully collocated storage arrangement for all transported properties. Within a structured non-orthogonal finite-volume system, the velocity vector is decomposed into its Cartesian components, and these are the components to which the momentum equations relate. Advective volume face fluxes are approximated by Leonard's QUICK scheme [25]. Mass continuity is enforced by solving a pressure-correction equation which, as part of the iterative sequence, steers the pressure towards a state at which all mass residuals in the cells are negligibly small. In conjunction with a fully collocated approach, this method is known to provoke chequerboard oscillations, reflecting a state of velocity-pressure decoupling. To avoid this, the widely used method of Rhie and Chow [26] is adopted to interpolate the cell face velocities from the nodal values. Physical diffusion fluxes are approximated by conventional second-order central differences.

## 4. Results and discussions

Meinders [4] and Meinders et al. [5] have made detailed measurements of the mean flow and turbulence using a two-component laser Doppler anemometer (LDA) system within an extensive array of cubes immersed in a two-dimensional plane channel flow. A total of 250 cubes of side length $H$ was placed in an aligned configuration consisting of 25 rows of 10 cubes each with cube spacings (face-to-face gaps) of $3H$ in both the streamwise and spanwise directions to give a frontal area density (i.e., ratio of frontal area of the cube to the lot area of the unit cell that contains the cube) of 0.0625. The depth of the plane channel is $3.4H$.

The geometry of the obstacle array is exhibited in Fig. 1. To simulate the flow in this array, we used a computational domain consisting of a sub-channel unit shown in Fig. 1. This sub-channel unit had dimensions of $4H \times 3.4H \times 4H$ for the LES calculations and $4H \times 3.4H \times 2H$ for the RANS calculations in the streamwise $x$, wall-normal $y$, and spanwise $z$ directions, respectively. A side view of the sub-channel unit showing five measurement locations is sketched in Fig. 2 in accordance with the Meinders et al. experiment [5]. These flow measurements were performed in a unit

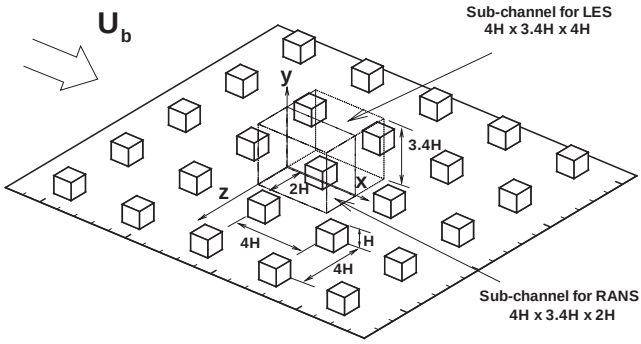


Fig. 1. A 3-D perspective view of a matrix of cubes.

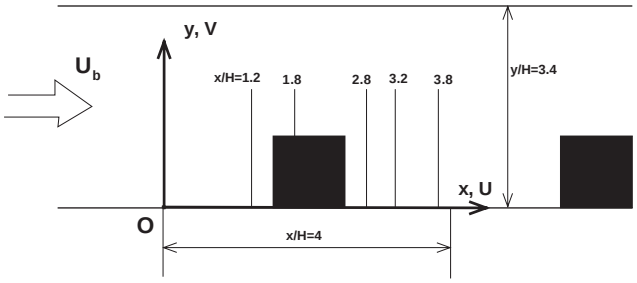


Fig. 2. A side view of a matrix of cubes in a bounded plane channel.

cell around the 18th row of the array. For this location, a fully developed and periodic state in the flow was achieved and the influences of both the inflow and outflow boundary conditions were eliminated.

Consistent with the experimental observations, the periodic boundary condition was used in the streamwise direction for both the LES and RANS computations. In the spanwise direction, a symmetry boundary condition was applied across the vertical center plane at $z = 0$ in the RANS calculations in order to reduce the computational cost. However, because the symmetry boundary condition about the $x$–$y$ plane at $z = 0$ is inappropriate for the instantaneous velocity field, a periodic boundary condition was applied across the pair of vertical boundary planes of the flow domain in the spanwise direction at $z = -2H$ and $z = 2H$ in the LES calculations. At the top and bottom walls of the channel, as well as at the surfaces of the cube, the no-slip and impermeability conditions were used in the LES calculations (for the tangential and wall normal velocity components, respectively) whereas the wall-function approach was utilized in the RANS calculations. In accordance with the experiment, the Reynolds number for all the simulations was 3800 based on the mean bulk velocity $U_b$ and the height $H$ of a cube.

The computational grids, consisting $48 \times 48 \times 48$ nodes in LES and $81 \times 60 \times 47$ nodes in RANS, were stretched preferentially near the top and bottom walls, as well as near the surfaces of the cube with a minimum grid spacing of about $0.03H$ for

both the LES and RANS calculations. Grid sensitivity study on RANS results was also conducted using a coarser grid of $41 \times 45 \times 32$ nodes. There was little difference in the predicted mean-flow and turbulence quantities between the fine- and coarse-grid RANS solutions. As a consequence, only the fine-grid solutions will be presented in this paper. Although no grid-dependence test was attempted in LES, it should be pointed out here that our LES results compare favorably well with other LES and DNS results presented at the 8th ERCOFTAC workshop on turbulence modeling (see tmdb.ws.tn.tudelft.nl/workshop8/case_2/case6_2.html).

In the LES approach, the profiles of mean velocity and turbulence statistics were obtained using a time-averaging (Reynolds-averaging) procedure. The initial condition for the streamwise velocity was assumed to have a mean value of $U_b$ with the initial streamwise (as well as spanwise and vertical) velocity fluctuations generated using a uniform random number generator to produce variates uniformly distributed in the interval $(-0.1U_b, 0.1U_b)$. After carrying out the simulation for several large-eddy turnover times $T_b \equiv H/U_b$ to ensure that the final time-averaged results were independent of the initial conditions, we averaged the instantaneous velocity over 4000 dimensionless time steps with a temporal resolution of $\Delta t/T_b = 1/32$ (corresponding to an averaging time of 125 large-eddy turnover time scales) to give the results for the mean velocity and turbulence statistics shown here. A simulation based on a longer averaging time of 12,000 dimensionless time steps at a finer temporal resolution of $\Delta t/T_b = 1/64$ (corresponding to an averaging time of 187.5 large-eddy turnover time scales) was also undertaken to ensure that the time-averaged quantities have statistically converged. It was found that the mean velocity and turbulence statistics obtained at the higher temporal resolution for the longer averaging time were almost identical to those obtained at the lower temporal resolution for the shorter averaging time. Hence, it is concluded that statistical convergence of the mean flow and turbulence quantities exhibited in this study is good (viz., long enough sampling or averaging times were used to ensure that the statistical quantities extracted were accurately determined). Because we used a staggered grid for the LES calculations, all mean flow and turbulence quantities correspond to averages at the centers of the computational cells.

To facilitate the discussion in the following subsections, the following abbreviations will be used:

(1) SMG: the standard Smagorinsky model;
(2) DMT: dynamic SGS model with time-averaging procedure;
(3) LDM: localized dynamic model;
(4) RANS: $k$–$\varepsilon$ model applied with standard wall functions;
(5) EXP: experimental data from [4].

### 4.1. Mean-velocity profiles

Fig. 3 shows the vertical profiles of the mean streamwise velocity obtained from the various numerical simulations compared with the experimental data in the $x$–$y$

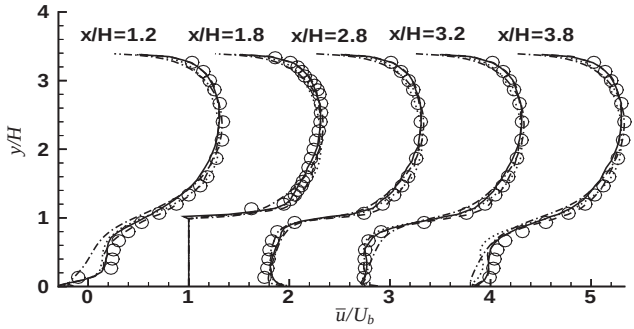


Fig. 3. Vertical profiles of the time-mean streamwise velocity on the vertical ($x$–$y$) plane through the center of the cube (i.e., at $z/H = 0$): —— LDM; - - - - DTM; ..... SMG; – · – RANS; ○ EXP. Note that each successive $x/H$-profile starting from the one at $x/H = 1.8$ has been offset by one unit from that of the previous $x/H$-profile for clarity of presentation.

plane at $z/H = 0$ (i.e., in the vertical center [symmetry] plane for the cube) at the five selected $x$-stations (i.e., at $x/H = 1.2,\ 1.8,\ 2.8,\ 3.2$ and 3.8) exhibited previously in Fig. 2. Note that the core flow in the region above the cube remains unidirectional, and that a reverse flow is present in the spanwise oriented street canyon between two rows of cubes. The latter implies the existence of a flow separation in the street canyon.

It is noted that agreement between the predicted and measured results of the streamwise mean velocity is generally very good (cf. Fig. 3). LDM gives the best conformance with the experimental observations at all the $x$-stations, and is seen to provide a remarkable overall agreement with the experimental results. At $x/H = 1.8$, a negative velocity peak at $y/H \approx 1$, implying the presence of a thin reverse flow in this region, is captured adequately by LDM. Note that although not supported directly by the velocity profile measurements at this station, it is evident from the flow visualization based on the surface streaklines that there exists a thin separation bubble on the rooftop of the cube originating from its upstream edge. For flow over a single cube (e.g., [7,3]), a similar reverse flow on the rooftop of the cube has also been noted in the experimental observations. Other numerical results obtained with DTM, SMG and RANS, however, do not capture any reverse flow at this location. For the RANS simulations (which utilized the standard $k$–$\varepsilon$ turbulence model), we did not attempt to re-calibrate the closure constants in order to improve the prediction of the mean flow at the leading edge of the cube rooftop.

Generally, SMG gives good results for the mean streamwise velocity compared to the experimental measurements, but somewhat under-predicts the mean flow in the region near the top wall ($y/H > 2.5$), and over-predicts the reverse flow, particularly at $x/H = 3.8$ in the street canyon downstream of and at $x/H = 1.2$ in the street canyon upstream of the cube. This is probably because the van Driest damping function introduced in Eq. (5), originating from a mixing-length model for boundary-layer flows, is inappropriate for the separated flows observed at these locations. Although DMT fails to predict the reverse flow on the rooftop of the cube

at $x/H = 1.8$, it does provide predictions for the streamwise mean velocity that are slightly better than those provided by LDM in the region $1 < y/H < 2$.

The results obtained with RANS conform reasonably well with LES results and experimental data for $y/H > 1$, but exhibit noticeable discrepancies for $y/H < 1$ in the street canyon. In particular, at $x/H = 1.2$ (which is upstream of the front face of the cube), RANS under-predicts significantly the streamwise mean velocity over the depth of the street canyon. This is consistent with the velocity vector plot shown later in Fig. 6 which indicates that RANS over-predicts the reattachment length of the separation bubble in the exit region, yielding a too slow flow recovery at $x/H = 1.2$. In a somewhat related study, Rodi [10] reports that for the flow over a single square cylinder in a free stream at $Re = 21,400$, the time-averaged reattachment length predicted by the standard $k$–$\varepsilon$ model is $l_R/H \approx 2.8$, which is significantly larger than the measured value of $l_R/H \approx 1.38$ obtained from the experiment.

Fig. 4 presents the horizontal profiles of the mean streamwise velocity on the $x$–$z$ plane at $y/H = 0.5$ (half cube height) at the same $x/H$-locations shown in Fig. 3. The flow between cubes in the spanwise direction ($z/H > 0.5$) is unidirectional, while the wake flow behind the cube is reversed for $2.5 < x/H < 3.8$. Overall, there is generally good agreement between the three LES results (i.e., LDM, DMT, and SMG) and the experimental measurements. Among these three LES computations, LDM is seen to generally provide the best conformance with $\bar{u}/U_b$ at all the $x$-stations. At $x/H = 1.8$, on the side wall of the cube at half cube height (i.e., at $y/H = 0.5$), a thin reverse flow is predicted only by LDM at this location. Evidence for the presence of this reverse flow region is supported by the flow visualization in the experiment (e.g., see Fig. 3 in [5]). In contrast, RANS gives consistently the poorest conformance with the experimental measurements for $\bar{u}/U_b$. In particular, the velocity profile on the side wall of the cube is too thick and maximum velocity occurs at $z/H = 2$ rather than at $z/H \approx 1$ as observed in the experiment. This is because RANS under-predicts significantly the velocity just upstream of the windward (front) face of the cube (e.g., at $x/H = 1.2$ as evident in Fig. 3). As the

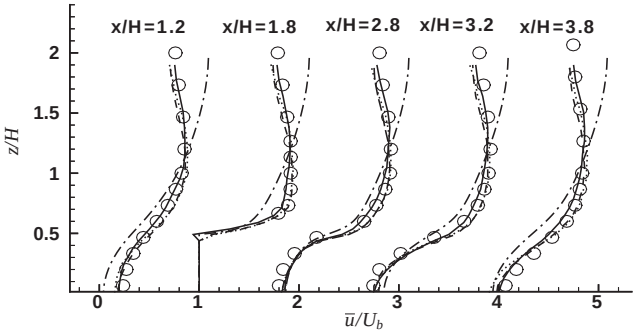


Fig. 4. Horizontal profiles of the time-mean streamwise velocity on the horizontal ($x$–$z$) plane at half cube height (i.e., at $y/H = 0.5$): —— LDM; - - - - DTM; ..... SMG; – · – RANS; ○ EXP. Note that each successive $x/H$-profile starting from the one at $x/H = 1.8$ has been offset by one unit from that of the previous $x/H$-profile for clarity of presentation.

low-momentum fluid passes around the cube, it tends to stay close to the side walls of the cube. As a consequence, the mean velocity at locations away from the walls must increase in order to maintain mass conservation, resulting in the prediction of a much greater mean velocity at $x/H = 1.8$, and also at $x/H = 1.2$, 2.8, 3.2 and 3.8 in the street canyon. One striking difference between RANS and LES predictions of the mean flow is evident in Fig. 4; namely, in the RANS prediction the mean streamwise velocity increases monotonically in the region between $z/H \approx 0.5$ and 2, whereas in the LES predictions, the mean streamwise velocity increases monotonically between $z/H \approx 0.5$ and 1 only, after which it begins to decrease between $z/H \approx 1$ and 2.

Fig. 5 displays predictions of the horizontal profiles of the mean spanwise velocity on the $x$–$z$ plane at $y/H = 0.5$ at the same $x/H$-locations as shown in the previous figure. The agreement between the LES results and the experimental measurements is generally fairly good. Among these predictions, it is noted that LDM still gives the best overall conformance with the measurements. All LES models fail to capture the negative velocity close to the side wall of the cube at $x/H = 1.8$, suggesting that all LES models under-predict the length of the separation bubble on the side wall emanating from the upstream vertical edge of the cube (albeit this flow feature is rather small).

It is encouraging to see that a near zero spanwise mean velocity component is predicted at $z/H = 0$ (vertical centerplane through the cube) and at $z/H = 2$ (vertical midplane between two adjacent cubes in the spanwise direction) in all three LES calculations in good conformance with the experimental measurements at these locations. This particular result indicates that the symmetry boundary condition in the mean velocity profile relative to the vertical symmetry planes at $z/H = 0$ and 2 has been satisfied to within numerical round-off errors. The center of the recirculation zone is estimated to be between $x/H = 2.8$ and 3.2 since the spanwise mean velocity component changes sign somewhere in this range. This is further supported by the velocity vector plot shown later in Fig. 9(a), in which the center of the recirculation zone is seen to be at $x/H \approx 3.1$. As in the case of the streamwise

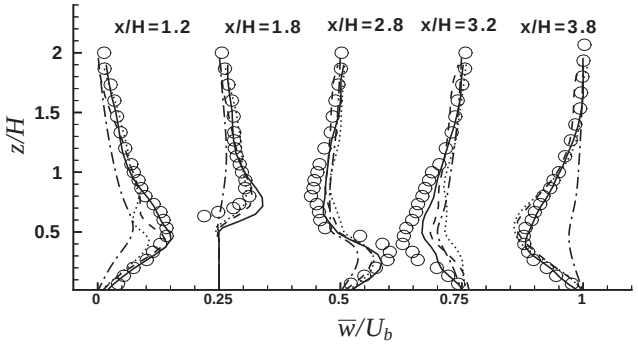


Fig. 5. Horizontal profiles of the time-mean spanwise velocity on the horizontal ($x$–$z$) plane at half cube height (i.e., at $y/H = 0.5$): —— LDM; - - - - DTM; ..... SMG; – · – RANS; ○ EXP. Note that each successive $x/H$-profile starting from the one at $x/H = 1.8$ has been offset by 0.25 unit from that of the previous $x/H$-profile for clarity of presentation.

mean velocity predictions on the same $x$–$z$ plane at $y/H = 0.5$ shown in Fig. 4, the performance of RANS is disappointing. Specifically, RANS under-predicts significantly the spanwise velocity component, particularly at $x/H = 1.8$, indicating that the flow is almost parallel to the side wall of the cube, and at $x/H = 3.8$, signifying that the curvature of the 2-D mean flow 'streamline' (based on the $\bar{u}$ and $\bar{w}$ velocity components only) emanating from the downstream vertical side edges of the cube at $x/H = 2.5$ is too small.

The time-averaged velocity vector fields on the $x$–$y$ plane at $z/H = 0$ (i.e., on the vertical center plane through the cube), obtained with the LDM and RANS models, are depicted in Fig. 6. The vortex structures in the proximity of the cube identified from both LDM and RANS predictions are very similar to those observed in the experiment (see Fig. 4 in [5]). A vortex with downwash velocities on the windward (front) face of the cube corresponding to the separation zone just upstream of the leading bottom edge of the cube is evident. Furthermore, a recirculation zone with strong upwash velocities close to the leeward (back) face of the cube that is dominated by an arch-shaped vortex in the wake region is clearly seen in the simulations.

Compared with experimental measurements, it is seen that LDM provides better predictions of the shapes and positions of the vortex cores than RANS. RANS predictions of the location (at $y/H \approx 0.35$) of the center of the vortex in front of the

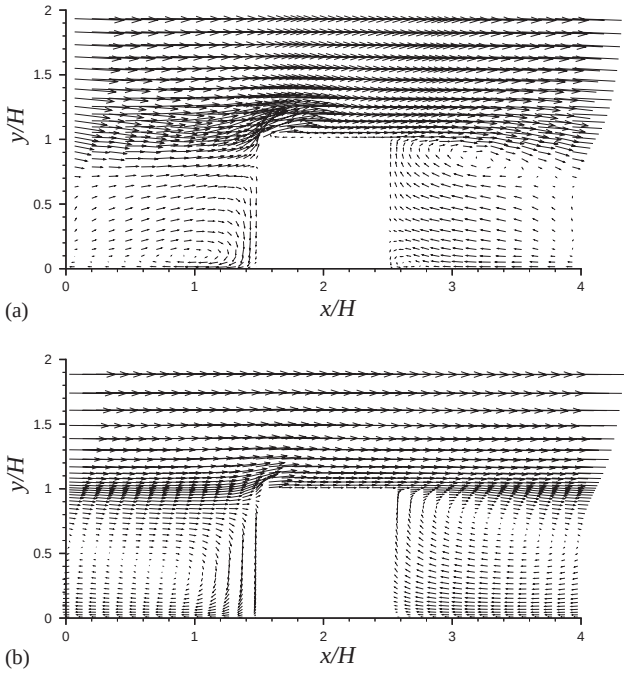


Fig. 6. The time-mean velocity vector field in the vertical ($x$–$y$) center plane of the cube obtained with (a) LDM and (b) RANS.

cube is too high and too far upstream (at $x/H \approx 0.8$) compared with the LDM prediction where the vortex core is at $(x/H, y/H) \approx (1, 0.1)$. As a result, LDM predicts a stronger velocity field within the recirculation region than RANS. LDM also captures a leading-edge separation bubble on the rooftop of the cube and a small corner vortex close to the bottom-downstream edge of the cube, which RANS completely fails to predict. Although the vector plot in Meinders et al.'s experiment does not indicate explicitly the existence of such a corner vortex, other studies for a flow over a single surface-mounted cube in a channel (e.g., [3]) did highlight the corner vortex structure in their reconstruction of the mean flow pattern.

The time-averaged velocity vector field on the vertical center symmetry plane at $z/H = 0$ is exhibited in Fig. 7. This figure displays explicitly the mean flow pattern within the spanwise oriented street canyon between two adjacent cubes separated in the streamwise direction. It is clear from this figure that the flow in the canyon is characterized by a two-cell vortex structure separated by the reattachment point of the upstream vortex at $x_R/H \approx 4.1$ (or at $1.6H$ downstream from leeward face of the upstream cube). The cube immediately downwind of this cube is seen to strongly disturb and interfere with the recirculating vortex close to the leeward face of the upstream cube.

Fig. 8 shows the time-averaged velocity field obtained with LDM in the canyon between two adjacent cubes on the $x$–$z$ planes at heights of $y/H = 0.25$, 0.50, and 0.75. The mean flow symmetry along the centerline at $z/H = 0$ is clearly produced by all the LES models (only LDM is shown here) at all three stations. A thin separation bubble on each of the side walls of the cube emanating from the vertical side edges at $x/H = 5.5$ is observed at the different $y/H$ vertical levels. At $y/H = 0.5$, for example, the reattachment length, $l_R$, predicted by LDM is about $0.3H$, which is in good agreement with the experimental value of $l_R \approx \frac{1}{3}H$. In the wake region, a pair of recirculation zones at different $y/H < 1$ form the "footprint" of an arch-type vortex identified in Meinders et al.'s experiment. It is seen from Fig. 8 that the recirculation area and, hence, the reattachment point $x_R$—identified as a point along the centerline at $z/H = 0$ where the mean streamwise velocity changes sign—increases

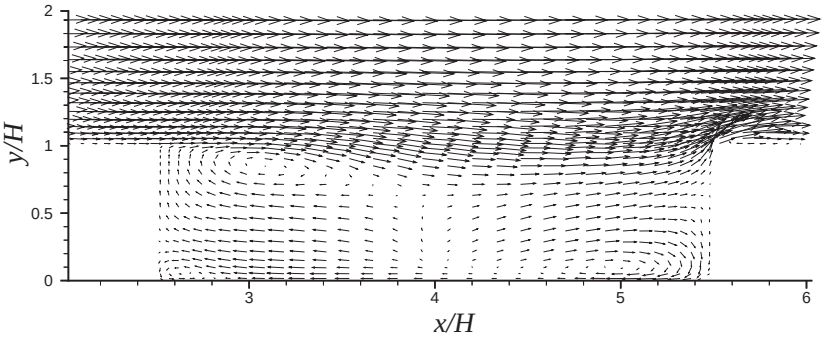


Fig. 7. The time-mean velocity vector field in the street canyon between two adjacent cubes in the vertical ($x$–$y$) center plane of the cubes obtained with LDM.

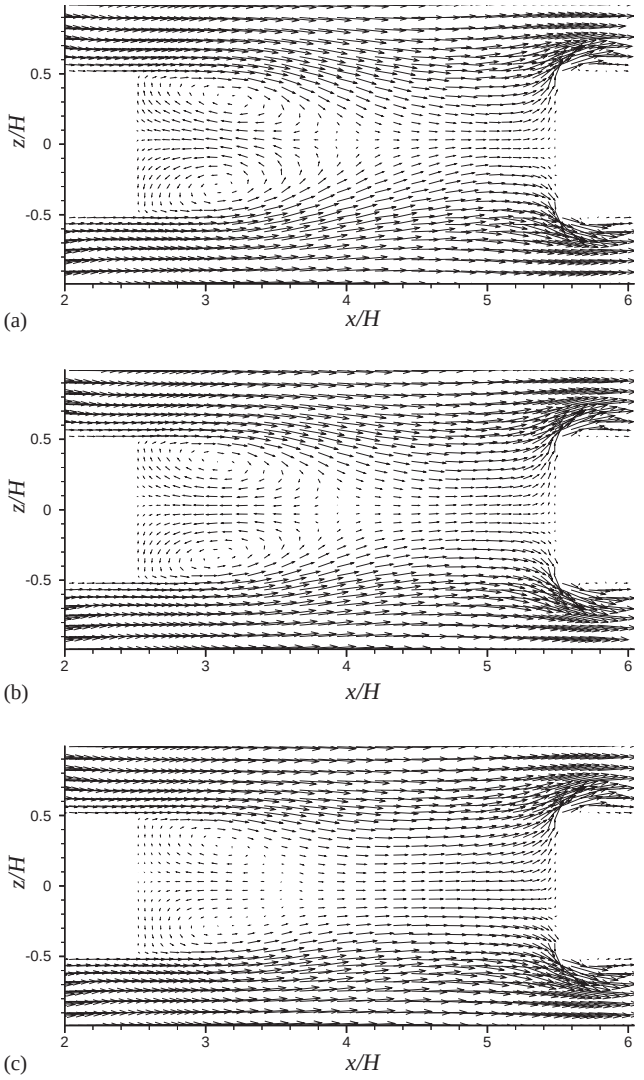


Fig. 8. The time-mean velocity vector field on the horizontal ($x$–$z$) plane at (a) $y/H = 0.25$, (b) 0.50, and (c) 0.75.

gradually from $y/H = 0.75$ to $y/H = 0.25$. At $y/H = 0.25$, LDM predicts $x_R/H = 4$, which corresponds well with the experimental value.

Comparison of the time-averaged velocity field obtained with LDM and RANS on the $x$–$z$ plane at $y/H = 0.5$ is exhibited in Fig. 9. Only one-half of the solution domain used in the LES calculations is shown here due to the satisfaction of the symmetry condition along the vertical center plane through the cube at $z/H = 0$ as already seen in Fig. 8. In the corridor region between two adjacent cubes in the

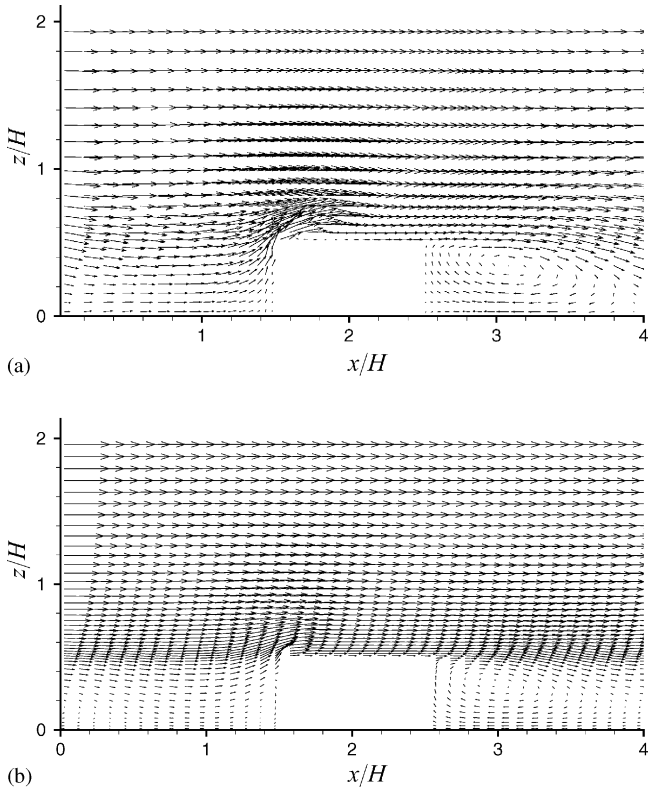


Fig. 9. The time-mean velocity vector field on the horizontal ($x$–$z$) plane at half cube height (i.e., at $y/H = 0.5$) obtained with (a) LDM and (b) RANS.

spanwise direction (i.e., in the streamwise oriented street canyon between two columns of cubes), the velocity vector is mostly parallel and undirectional except close to the upstream side edge of the cube at $x/H = 1.5$ and in the wake region where $x/H > 2.5$. The mean streamwise velocity in front of the cube predicted by RANS is significantly smaller than that obtained by LDM due to an overestimation of the recirculation length upstream of the cube in the RANS calculation. Consequently, the low-momentum fluid in the stagnation region in front of the cube is easier to deflect away from the streamwise direction, yielding a larger turning angle around the vertical side edge of the cube. Hence, RANS overpredicts the mean streamwise velocity, as shown earlier in Fig. 4, and fails to capture the leading-edge separation bubble on the side wall.

### 4.2. Reynolds stresses

Fig. 10 shows the streamwise Reynolds normal stress, $\overline{u'^2}$, on the $x$–$y$ plane at $z/H = 0$ (vertical profiles) and on the $x$–$z$ plane at $y/H = 0.5$ (horizontal profiles) at

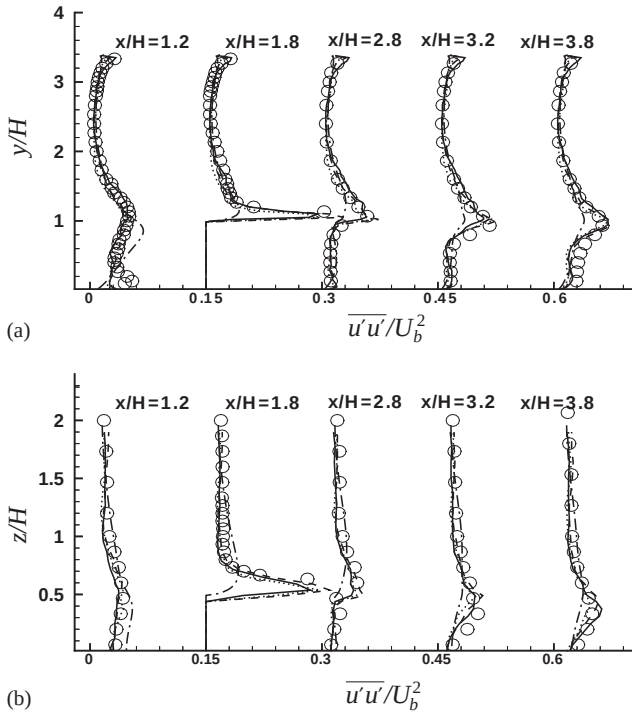


Fig. 10. Profiles of streamwise Reynolds normal stress on (a) the vertical ($x$–$y$) plane through the center of the cube (i.e., at $z/H = 0$) and (b) the horizontal ($x$–$z$) plane at half cube height (i.e., at $y/H = 0.5$): —— LDM; - - - - DMT; ..... SMG; – · – RANS; ○ EXP. Note that each successive $x/H$-profile starting from the one at $x/H = 1.8$ has been offset by 0.15 unit from that of the previous $x/H$-profile for clarity of presentation.

five selected $x/H$-stations shown in Fig. 2. The peak value of $\overline{u'^2}$ at each $x$-station occurs at $y/H \approx 1$ on the $x$–$y$ plane at $z/H = 0$, and at $z/H \approx 0.5$ on the $x$–$z$ plane at $y/H = 0.5$, respectively. These observed peaks in $\overline{u'^2}$ correspond to the generation and development of the thin intense vertical and horizontal shear layers along the rooftop and side walls of the cube, respectively. The maximum value of $\overline{u'^2}$ is found on the rooftop and side walls of the cube (i.e., at $x/H = 1.8$). Moving downstream of this position, the evolution of $\overline{u'^2}$ in a vertical plane along the cube centerline or in a horizontal plane at half cube height is dominated by the vertical or horizontal spreading, respectively, of the vertical or horizontal shear layers generated at the rooftop and side walls of the cube. As a consequence, the peak value of $\overline{u'^2}$ attenuates downstream as the streamwise normal stress is "exported" by outward pressure or turbulent transport from the center of the vertical or horizontal shear layers.

The agreement between predictions provided by the three LES models and the corresponding experimental measurements is, in general, good with the exception of the $\overline{u'^2}$ values close to the wall at $x/H = 1.2$ shown in Fig. 10(a). This small disagreement might be due to insufficient grid resolution or experimental error. The

RANS predictions for $\overline{u'^2}$, on the other hand, exhibit noticeable discrepancy from the experimental measurements. In particular, the peak values of $\overline{u'^2}$ at each $x$-station in the vertical plane along the cube centerline and in the horizontal plane at half cube height are significantly underestimated except at $x/H = 1.2$ (i.e., in the impact region or impingement zone of the cube) where the peak value of $\overline{u'^2}$ is overestimated. Furthermore, at $x/H = 1.8$, the maximum values of $\overline{u'^2}$ in the $x$–$y$ plane at $z/H = 0$ and in the $x$–$z$ plane at $y/H = 0.5$ are about 60% lower than those obtained from the LES predictions, the latter of which agrees well with the experimental measurements. Finally, it is noted that on the rooftop of the cube, LDM predicts correctly the peak value of $\overline{u'^2}$, while SMG and DMT slightly overpredict this value.

A comparison of the spanwise Reynolds normal stress, $\overline{w'^2}$, on the $x$–$y$ plane at $z/H = 0$ (vertical profiles) and the $x$–$z$ plane at $y/H = 0.5$ (horizontal profiles), obtained from the LES and RANS calculations with the corresponding experimental measurements is shown in Fig. 11. Good agreement of $\overline{w'^2}$ with the experimental results is obtained with LDM, DTM, and SMG for $y/H > 1$ [cf. Fig. 11(a)] and for $z/H > 0.5$ [cf. Fig. 11(b)]. In the wake region, however, all LES models underpredict the magnitude of $\overline{w'^2}$. Among these LES models, however, it is seen that LDM still

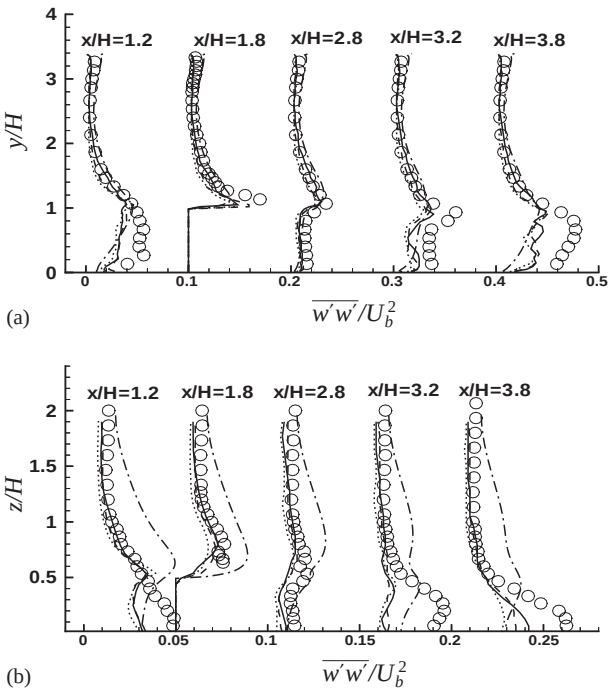


Fig. 11. Profiles of spanwise Reynolds normal stress on (a) the vertical ($x$–$y$) plane through the center of the cube (i.e., at $z/H = 0$) and (b) the horizontal ($x$–$z$) plane at half cube height (i.e., at $y/H = 0.5$): —— LDM; - - - - DTM; ..... SMG; – · – RANS; ○ EXP. Note that each successive $x/H$-profile in (a) and (b) starting from the one at $x/H = 1.8$ has been offset by 0.1 and 0.05 unit, respectively, from that of the previous $x/H$-profile for clarity of presentation.

provides the best conformance with $\overline{w'^2}$, particularly along the centerline of the cube in the horizontal (i.e., $x$–$z$) plane at half cube height (i.e., at $y/H = 0.5$). In order to identify the source of the problem with respect to the prediction of $\overline{w'^2}$ in the wake region, we doubled the size of the sub-channel unit in either the streamwise (or, $x$-) and spanwise (or, $z$-) directions. Even with a larger computational domain, the discrepancy between LES model predictions of $\overline{w'^2}$ and the corresponding measured values in the wake region remains. Currently, this is an unresolved issue requiring further investigation. Not too surprisingly, the RANS predictions for $\overline{w'^2}$, particularly in the horizontal plane at half cube height [cf. Fig. 11(b)] are generally very poor. The limitation of RANS for capturing complex vortex structures is readily apparent here.

Fig. 12 exhibits the Reynolds shear stress $\overline{u'w'}$ on the $x$–$z$ plane at $y/H = 0.5$. The location of the peak value in the measured Reynolds shear stress approximately coincides with the separation line which emanates from the leeward vertical side edge of the cube (see Fig. 9) where the mean shear strain $\bar{S}_{13} \equiv \frac{1}{2}((\partial\bar{u}/\partial z) + (\partial\bar{w}/\partial x))$ is a maximum, and which reattaches at $x/H \approx 4$ along the cube centerline (i.e., along $z/H = 0$). The peak value location of $\overline{u'w'}$ at $x/H = 3.8$ (i.e., at a position slightly upstream of the reattachment point) in the horizontal plane at half cube height occurs at $z/H \approx 0.25$ for the LDM prediction which accords well with the experimental results. Furthermore, the magnitude of the $\overline{u'w'}$ peak value is also well predicted by the LDM calculations here. In contrast, the peak value of $\overline{u'w'}$ predicted by RANS at the same downstream location (i.e., at $x/H = 3.8$) is smaller than the measured value implying that entrainment of fluid into the recirculation zone is reduced. As a result, the spanwise location of the peak of $\overline{u'w'}$ provided by the RANS calculation is significantly greater (at $z/H \approx 0.5$), yielding an overestimation of the reattachment length. Fig. 12 also shows that the magnitude of $\overline{u'w'}$ obtained from the RANS calculation is generally larger than both the LES predictions and the experimental measurements for $z/H > 0.5$ (i.e., in the streamwise oriented street canyons between the cubes). This is consistent with the streamwise mean velocity

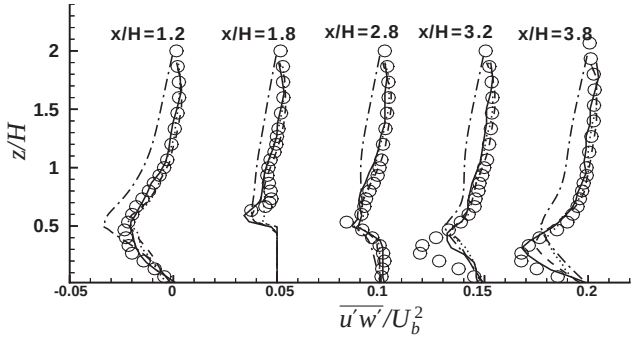


Fig. 12. Horizontal profiles of Reynolds shear stress on the horizontal ($x$–$z$) plane at half cube height (i.e., at $y/H = 0.5$): —— LDM; ---- DTM; ..... SMG; – · – RANS; ○ EXP. Note that each successive $x/H$-profile starting from the one at $x/H = 1.8$ has been offset by 0.05 unit from that of the previous $x/H$-profile for clarity of presentation.

profiles shown in Fig. 4, in which $\bar{S}_{13}$ ($\sim|\overline{u'w'}|$, in accordance with a linear eddy-viscosity model) predicted by the RANS model is also found to be larger than the corresponding measured values in the same region.

### 4.3. Turbulence energy

Contours of the turbulence kinetic energy (TKE), $k \equiv \frac{1}{2}(\overline{u'^2} + \overline{v'^2} + \overline{w'^2})$, in the $x$–$y$ plane at $z/H = 0$, are presented in Fig. 13 for the LDM (upper figure) and RANS (lower figure) calculations, respectively. Note that $k$ is relatively small in the core region and increases gradually towards the top wall of the channel where shear

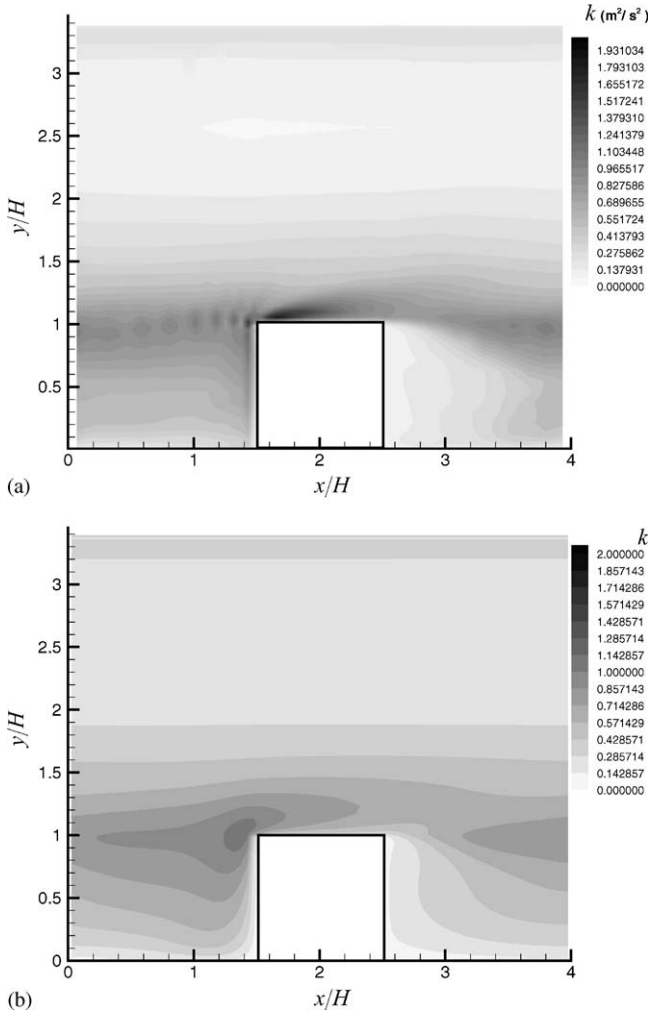


Fig. 13. Contours of the turbulence kinetic energy $k \equiv \frac{1}{2}(\overline{u'^2} + \overline{v'^2} + \overline{w'^2})$ in the vertical ($x$–$y$) center plane through the cube obtained with (a) LDM and (b) RANS.

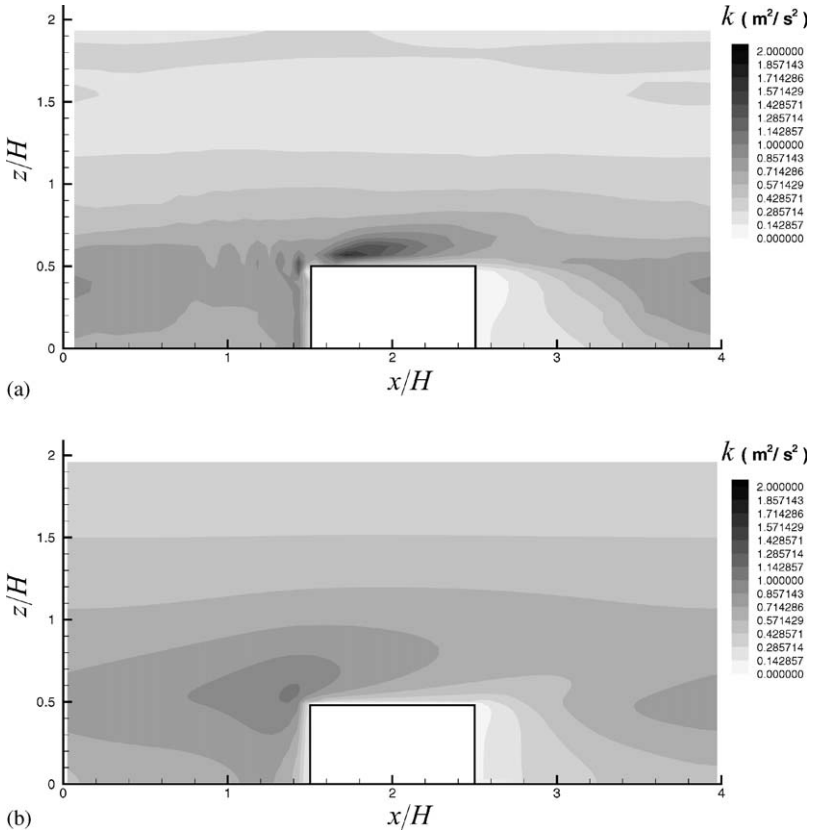


Fig. 14. Contours of the turbulence kinetic energy $k \equiv \frac{1}{2}(\overline{u'^2} + \overline{v'^2} + \overline{w'^2})$ in the horizontal ($x$–$z$) plane at half cube height (i.e., at $y/H = 0.5$) obtained with (a) LDM and (b) RANS.

production of TKE increases. A high level of $k$ is seen to occur at the leading edge of the rooftop of the cube where a thin separation bubble occurs (see also Fig. 6). This turbulence energy is subsequently advected downstream with the position of its maximum following approximately the separation line, emanating from the leeward rooftop edge of the cube, where the shear-strain rate is high. Another region with an increased level of $k$ occurs on the front (windward) face of the cube, where a narrow 'tail' of $k$ originating at the windward edge of the cube rooftop is deflected downwards in the region $0.3 < y/H < 1.1$ due to impingement of the flow on the cube. One interesting flow feature seen in the TKE contours predicted by LDM is the presence of localized regions (i.e., small core regions) with large TKE levels resulting from unstable vortex structures distributed along the thin shear layer near the rooftop level of the cubes (i.e., at $y/H = 1$) extending approximately from the middle of the street canyon at $x/H \approx 3.8$ to the front face of the cube immediately downstream of it.

The $k$-contours from the RANS prediction are noticeably different than the LDM prediction and the experimental results, particularly near the windward rooftop edge of the cube, along the curved shear layer bordering the thin separation zone on the rooftop, and in the impingement region upstream of the front face of the cube. The maximum levels of $k$ in these regions are generally found to be lower for the RANS prediction than for the LDM prediction. Furthermore, the unstable vortex structures mentioned previously with reference to the LDM prediction are not present in the RANS results. This should not be too surprising because steady RANS predictions cannot account for the presence of these unsteady vortex structures in the flow.

Fig. 14 displays TKE contours on the $x$–$z$ plane at $y/H = 0.5$. The local maxima of $k$ within the separation zones on the side walls of the cube are evident in the LDM simulation. In contrast, the RANS simulation under-predicts the turbulence energy in the impingement region due to an overestimation of the recirculation zone and, hence, results in a too slow flow recovery in the wake region.

### 4.4. Energy spectra

Figs. 15 and 16 display the energy spectra for the streamwise, vertical, and spanwise velocity components obtained from the LDM and DMT simulations, respectively. These energy spectra were evaluated at $(x/H, y/H, z/H) = (2, 1.28, 0)$. The energy spectra for the streamwise ($u$) and vertical ($v$) velocity components appear to exhibit an inertial subrange spanning about one decade in frequency range from about 0.3 to about 3 Hz, where the spectra exhibit a slope close to $-\frac{5}{3}$ predicted by Kolmogorov theory. This implies that our LES simulations have adequately resolved most of the energy present in the turbulent scales of the flow for these two velocity components. Because most of the energy in the flow has been resolved, it is expected that the characteristics of the dominant flow features predicted by the various LES simulations (at least for the streamwise and vertical velocity) should be nearly independent of the details of the subgrid closure. This is consistent with our previous observation that the important or dominant flow structures for the streamwise velocity component are adequately predicted by all three subgrid closure models used in this study. If the computational grid is fine enough (as it appears to be in this study) to represent (or, resolve) the dynamics of the dominant vortex structures in the flow, then it is expected that the characteristics of the subgrid models employed should not alter significantly these dynamical flow features.

Interestingly, the energy spectra for the spanwise ($w$) velocity component does not appear to exhibit an inertial subrange. It is possible that the formation of an inertial subrange here is obviated by the pronounced inhomogeneities that are present in the current complex flow, but this seems unlikely given the presence of inertial subranges in the energy spectra for the streamwise and vertical velocity components. Alternatively, it is possible that the filter width (and, hence, grid size) used in the discretization of the flow domain in the spanwise direction is too coarse, implying that the smallest resolved eddies in the spanwise direction for our simulation do not

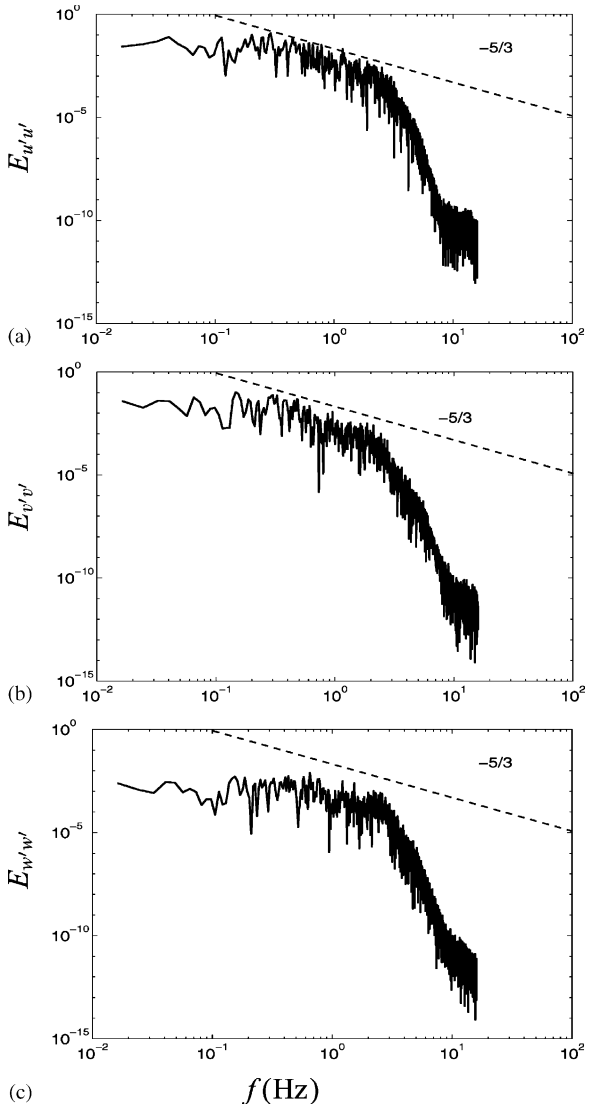


Fig. 15. Time energy spectra obtained from LDM model for the (a) streamwise velocity component, (b) vertical velocity component, and (c) spanwise velocity component. These energy spectra were evaluated at $(x/H, y/H, z/H) = (2, 1.28, 0)$.

fall within the inertial subrange [viz., the discretization is too coarse in the spanwise direction to resolve scales that exhibit local isotropy (approximately or better)]. This may imply that the subgrid scale energy in the spanwise direction may be significant and provide an explanation for the discrepancies in the predictions of $\overline{w'^2}$ shown in Fig. 11.

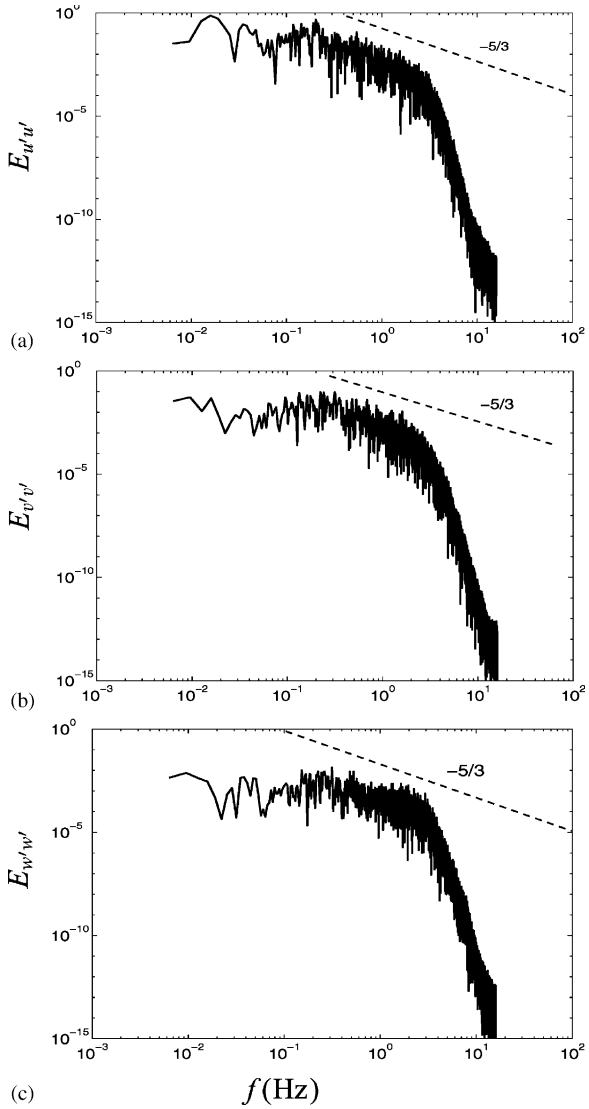


Fig. 16. Time energy spectra obtained from DMT model for the (a) streamwise velocity component, (b) vertical velocity component, and (c) spanwise velocity component. These energy spectra were evaluated at $(x/H, y/H, z/H) = (2, 1.28, 0)$.

## 5. Conclusions

Three variants of SGS models for LES (namely LDM, DMT, and SMG) that are applicable to inhomogeneous flows and a RANS model (namely, the standard $k$–$\varepsilon$ model used with wall functions) were applied to compute a fully developed turbulent

flow over a matrix of cubes in a plane channel. Detailed comparisons between the numerical predictions obtained with the LES and RANS models and the corresponding experimental data of Meinders et al. were conducted. The results of this investigation allow the following conclusions to be drawn:

(1) Flow structures observed in the experiment, including a horseshoe vortex at the front face of the cube that wraps around the side walls, an arch-shaped vortex in the wake, and thin separation bubbles on the rooftop and side walls originating from the leading (windward) edge of the roof and the vertical edges of the side walls, respectively, were captured reasonably well by all the models. Among these models, LDM was found to give the best conformance with the detailed experimental measurements and is the only model, examined here, that was capable of predicting the separation/reattachment processes on all the surfaces of the cube.

(2) Quantitatively, the profiles of mean velocities and Reynolds stresses, the latter including $\overline{u'^2}$, $\overline{w'^2}$ and $\overline{u'w'}$, are generally well represented by all the LES models. The greatest discrepancy between the predictions and observations was for $\overline{w'^2}$ within the street canyons of the obstacle array. Increasing the size of the sub-channel unit by doubling the dimensions in either the streamwise or spanwise directions did not yield any better predictions for $\overline{w'^2}$ within the street canyons. The generally poor prediction of $\overline{w'^2}$ in the street canyons will require further investigation. Nevertheless, the accuracy of the predictions is generally higher for the LDM model than for any of the other subgrid models considered.

(3) The RANS results (more specifically, predictions provided by the standard $k$–$\varepsilon$ model) were found to be considerably different from the LES predictions and the experimental measurements. The size of the recirculation zone in the wake of the upstream cube—as part of the arch-shaped vortex—is overestimated in the RANS simulation. This leads to a severe underestimation of the mean streamwise velocity component in the horseshoe vortex region just upstream of the lower part of the front face of the downstream cube. This, in turn, creates much thicker boundary layers on the side walls of the cube in the spanwise direction as the flow passes around the sides of the cube.

(4) In addition to the standard $k$–$\varepsilon$ model used in this study, the Kato–Launder [11] model, which was designed specifically to reduce the turbulence-energy anomaly in the impingement region, was also used to simulate the current flow (not shown). However, for the current fully developed flow the effect of the modification introduced to the turbulence generation term in the Kato–Launder model is small, with the result that this model yielded predictions of the mean velocity that was virtually identical to those obtained with the standard $k$–$\varepsilon$ model. In consequence, only results obtained with the standard $k$–$\varepsilon$ model were presented here.

(5) The complex features (e.g., vortex shedding, large separation zones, topology of the reattachment lines bordering the recirculation regions, fine-scale flow structures near the side walls, etc.) of the fully developed flow within and above an array of cubes are reproduced better with LES calculations than with RANS

calculations, albeit at the disadvantage of much greater computation times. In the present study, the computational cost associated with LES is about 100 times greater than that incurred with the $k$–$\varepsilon$ RANS model.

## Acknowledgements

The financial support of the Industrial Research Fellowship (IRF) for the first author from NSERC is gratefully acknowledged. The authors also acknowledge Dr. Frank Ham's guidance in using his LES code for the present research.

## References

[1] S. Becker, H. Lienhart, F. Durst, Flow around three-dimensional obstacles in boundary layers, J. Wind Eng. Indus. Aerodyn. 90 (2002) 265–279.
[2] I.P. Castro, A.G. Robins, The flow around a surface-mounted cube in uniform and turbulent streams, J. Fluid Mech. 79 (1977) 307–355.
[3] R. Martinuzzi, C. Tropea, The flow around surface-mounted, prismatic obstacles placed in a fully developed channel flow, J. Fluids Eng. 115 (1993) 85–92.
[4] E.R. Meinders, Experimental study of heat transfer in turbulent flows over wall-mounted cubes, Ph.D. Thesis, Faculty of Applied Sciences, Delft University of Technology, Delft, Netherlands, 1998.
[5] E.R. Meinders, K. Hanjalic, Vortex structure and heat transfer in turbulent flow over a wall-mounted matrix of cubes, Int. J. Heat Fluid Flow 20 (1999) 255–267.
[6] URL Available: http://tmdb.ws.tn.tudelft.nl/workshop8/case6_2/case6_2.html
[7] S. Murakami, A. Mochida, K. Hibi, Three-dimensional numerical simulation of air flow around a cubic model by means of large Eddy simulation, J. Wind Eng. Indus. Aerodyn. 25 (1987) 291–305.
[8] H. Werner, H. Wengle, Large Eddy simulation of turbulent flow over and around a cube in a plane channel, in: U. Schumann et al. (Eds.), Proceedings of the Eighth Symposium on Turbulent Shear Flows, Springer, Berlin, 1993.
[9] D. Lakehal, W. Rodi, Calculation of the flow past a surface-mounted cube with two-layer turbulence models, J. Wind Eng. Indus. Aerodyn. 67,68 (1997) 65–78.
[10] W. Rodi, Comparison of LES and RANS calculation of the flow around bluff bodies, J. Wind Eng. Indus. Aerodyn. 69–71 (1997) 55–75.
[11] M. Kato, B.E. Launder, The modeling of turbulent flow around stationary and vibrating square cylinders, Proceedings of the Ninth Symposium on Turbulent Shear Flows, Kyoto, Japan, 1993.
[12] T. Cebeci, A.M.O. Smith, Analysis of Turbulent Boundary Layers, Academic Press, New York, 1974.
[13] M. Germano, U. Piomelli, P. Moin, W.H. Cabot, A dynamic subgrid-scale eddy viscosity model, Phys. Fluids A 3 (1991) 1760–1765.
[14] D.K. Lilly, A proposed modification of the Germano subgrid scale closure method, Phys. Fluids A 4 (1992) 633–635.
[15] K. Akselvoll, P. Moin, Large Eddy simulation of a backward facing step flow, in: W. Rodi, et al., (Eds.), Engineering Turbulence Modeling and Experiments, Vol. 2, Elsevier Science Publishers BV, Amsterdam, 1993, pp. 303–313.
[16] M. Breuer, W. Rodi, Large-Eddy simulation of turbulent flow through a straight square duct and a 180° bend, Direct and Large-Eddy Simulation, Vol. I, Kluwer Academic Publishers, Dordrecht, 1994, 273–285.
[17] U. Piomelli, J. Liu, Large Eddy simulation of rotating channel flows using a localized dynamic model, Phys. Fluids A 7 (1995) 839–848.
[18] S. Ghosal, T.S. Lund, P. Moin, K. Akselvoll, A dynamic localization model for large Eddy simulation of turbulent flow, J. Fluid Mech. 286 (1995) 229–255.

[19] E.R. Meinders, T.H. Vandermeer, K. Hanjalic, Local convective heat transfer from an array of wall-mounted cubes, Int. J. Heat Mass Transfer 41 (1998) 335–346.
[20] Y. Morinishi, T.S. Lund, O.V. Vasilyev, P. Moin, Fully conservative higher order finite difference schemes for incompressible flow, J. Comput. Phys. 143 (1998) 90–124.
[21] F.E. Ham, F.S. Lien, A.B. Strong, A fully conservative second-order finite difference scheme for incompressible flow on nonuniform grids, J. Comput. Phys. 177 (2002) 117–133.
[22] S.P. Vanka, A calculation procedure for three-dimensional steady recirculating flows using multigrid methods, Comput. Meth. Appl. Mech. Eng. 55 (1986) 321–338.
[23] F.E. Ham, F.S. Lien, A.B. Strong, Efficient direct numerical simulation using multigrid with dynamic semi-coarsening, Proceedings of the Seventh Annual Conference of the Computational Fluid Dynamics Society of Canada, Halifax, Nova Scotia, Canada, 1999.
[24] F.S. Lien, M.A. Leschziner, A general non-orthogonal collocated finite volume algorithm for turbulent flow at all speeds incorporating second-moment closure, Part 1: numerical implementation, Comput. Meth. Appl. Mech. Eng. 114 (1994) 123–148.
[25] B.P. Leonard, A stable and accurate convective modeling procedure based on quadratic upstream interpolation, Comput. Meth. Appl. Mech. Eng. 19 (1979) 59–98.
[26] C.M. Rhie, W.L. Chow, Numerical study of the turbulent flow past an airfoil with trailing edge separation, AIAA J. 21 (1983) 1525–1532.